ADVANCED FUNCTIONAL MATERIALS
www.afm-journal.de

Dielectric Engineering of Perovskite $BaMnO_3$ for the Rapid Heterogeneous Nucleation of Pt Nanoparticles for Catalytic Applications

Lucia Hughes, Ahin Roy, Neelam Yadav, Clive Downing, Michelle P. Browne, Jagdish K. Vij, and Valeria Nicolosi**

Microwave heating provides a rapid method for the heterogeneous nucleation of noble metal particles on perovskite support materials for electrocatalytic purposes. To succeed, dielectric tuning of perovskite materials becomes fundamental. Herein, the dielectric engineering of the $BaMnO_3$ perovskite system is carried out through the use of B-site doping to give $BaTi_{0.5}Mn_{0.5}O_3$. Using a combination of atomic-scale imaging and electron energy loss spectroscopy (EELS), the preferential filling of the M1 and M3 B-sites with Mn and Ti ions in the 12R-rhombohedral perovskite structure is established. While the addition of Ti in the $BaMnO_3$ system has no detrimental effects on the presence of the oxygen reduction reaction (ORR) active Mn^{3+} states at the surface, it does alter the dielectric constant and loss tangent, thus facilitating the heterogeneous nucleation of Pt nanoparticles on $BaTi_{0.5}Mn_{0.5}O_3$ via rapid microwave heating. Higher Pt loading regimes are found to increase the size and aggregation of the nucleated particles, thus reducing their ORR activity. Therefore, lower Pt loading not only reduces costs but improves overall activity. This work represents future possibilities for the dielectric engineering of perovskite and similar support materials to aid in the quick and easy formation of stable noble metal-support catalytic systems.

1. Introduction

Driven by the growing energy demand of the Earth's population and the concerns about global warming, today's scientists are challenged with the development of renewable and efficient energy production and storage technologies. One of the key pieces in this puzzle is the discovery and design of catalyst materials to improve the efficiency of energy conversion devices, such as fuel cells, electrolytic water-splitting devices, and metal-air batteries.[1–3] The oxygen reduction reaction (ORR) is one of the main processes at the heart of fuel cell technologies, however, its slow kinetics also mean that it is considered the key bottleneck in their performance.[4,5] As a result, many efforts have been made in search of desirable electrocatalysts that can compensate for the loss of cell efficiency by overcoming the slow kinetics of the ORR. This would subsequently facilitate the practical

L. Hughes, V. Nicolosi
Centre for Research of Adaptive Nanostructures and Nanodevices (CRANN) & Advanced Materials and Bioengineering Research Centre (AMBER)
Trinity College Dublin
Dublin 2, Dublin D02, Ireland
E-mail: hugheslu@tcd.ie; nicolov@tcd.ie

L. Hughes, C. Downing, V. Nicolosi
Advanced Microscopy Laboratory
Trinity College Dublin
Dublin 2, Dublin D02, Ireland

L. Hughes, V. Nicolosi
School of Chemistry
Trinity College Dublin
Dublin 2, Dublin D02, Ireland

A. Roy
Material Science Centre
Indian Institute of Technology Kharagpur
Kharagpur 721302, India

N. Yadav, J. K. Vij
Department of Electronics and Electrical Engineering
Trinity College Dublin
Dublin 2, Dublin D02, Ireland

M. P. Browne
Helmholtz-Zentrum Berlin für Materialien und Energie
14109 Berlin, Germany

The ORCID identification number(s) for the author(s) of this article can be found under https://doi.org/10.1002/adfm.202402103

DOI: 10.1002/adfm.202402103

and widespread use of fuel cell technologies, which include proton exchange membrane fuel cells and alkaline fuel cells.[6,7]

So far, Pt and Pt-based catalysts have formed the benchmark for ORR catalysis owing to their high electrocatalytic activity, excellent work function, and high exchange current density.[8–12] However, the high expense, low availability, and low durability associated with Pt limits its extensive commercialization. Catalyst stability plays an additional critical factor in cell performance, as Pt catalysts suffer from dissolution, aggregation, and sintering during use.[13,14] As a result, electrodes for fuel cell technologies are usually formed by depositing Pt on a support material to prevent aggregation and the decrease in electro-active surface area. Typically, carbon black is utilized as the support material due to its high conductivity and porosity.[15] However, its stability causes limitations, as carbon-based supports are subject to corrosion in the extreme conditions associated with fuel cells.[16–18] Consequently, attention has turned to the development of robust non-carbon support materials, of which metal oxides, including perovskites, serve as suitable candidates due to their structural and compositional flexibility, tunable reactivity, and high stability.[19–23]

Unlike carbon-based supports, perovskites can display their catalytic activity.[3,24–26] Thus, the decoration of Pt nanoparticles on their surfaces acts to add to their inherent activity, rather than acting as the sole source of ORR activity. Further to this, the synergistic co-catalytic effects between Pt and the metal oxide support, often termed strong metal-support interactions (SMSI), can further enhance the catalytic activity of the system due to partial charge transfer or structural changes within the Pt particles.[23,27–29] Mesokinetic studies on supported Pt catalysts have shown that the microscopic geometric and electronic properties of the Pt active sites are key factors in determining the resulting macroscopic catalytic properties.[30,31] Consequently, the combination of Pt nanoparticles on perovskite supports allows for a large number of active sites and high intrinsic activity, both of which are crucial for achieving high rates of oxygen turnover at the cathode, ensuring high fuel cell power density. In saying that, it is important to keep the cost and scarcity of Pt in mind, meaning catalyst optimization must involve minimizing Pt loading.

The nucleation of Pt nanoparticles on the surface of support materials can be achieved at relatively low temperatures and short heating times using microwave heating.[32,33] Such methods are highly dependent on the processes through which homogeneous nucleation and heterogeneous nucleation occur, where the former results in the nucleation of particles in solution, and the latter results in the nucleation of particles on the support material. Heterogeneous nucleation is favored when the temperature of the support is higher than the temperature of the solution (assuming the temperature exceeds that required for heterogeneous nucleation).[32] When radiated with microwave radiation, the power absorbed per unit volume of a material is given by

$$P_v = 2\pi f \varepsilon_0 \varepsilon' \tan\delta E_{rms}^2 \quad (1)$$

where f and E_{rms} are the frequency and root mean square electric field of the microwave radiation, ε_0 is the permittivity of free space, ε' is the real part of the material's complex dielectric permittivity, and tan δ is its loss tangent.[34] Therefore, the power absorbed by a material is highly dependent on its dielectric properties, and hence, the dielectric engineering of perovskite materials proves vital in promoting the nucleation and dispersed loading of Pt nanoparticles at their surfaces.

For the Pt-perovskite catalyst system, there are several complex factors at play when optimizing performance. Pt particle size and surface area control, as well as perovskite e_g orbital filling, and defect chemistry tuning, are all crucial factors in governing the resulting electrocatalytic activity.[35,36] Our previous report on the perovskite material $BaMnO_3$, used scanning transmission electron microscopy (STEM) imaging in combination with electron energy loss spectroscopy (EELS) to reveal the presence of reduced Mn surface states in $BaMnO_3$, which ultimately formed the source of the material's ORR activity.[37] While this study acts as an extension of our past report, it explores a new electrocatalytic system by focusing on the nucleation of Pt nanoparticles on the perovskite surface to form a stable hybrid ORR electrocatalyst, and thus further optimize ORR performance of the perovskite system. Leveraging the flexibility of the perovskite system, we introduce B-site doping of $BaMnO_3$ using Ti, to tune the dielectric properties of the material and promote the heterogeneous nucleation and stabilization of Pt nanoparticles at its surface. As is the case for any practical energy conversion technology, the fundamental understanding and rational design of the electrocatalyst material is essential. To fulfill this requirement, atomic-resolution STEM imaging, EELS, and energy dispersive X-ray spectroscopy (EDX) are used to investigate the surface structure and composition of the $BaTi_xMn_{1-x}O_3$ perovskite, as well as the hybrid catalyst system. The findings in this study provide atomic-scale evidence for the structure and B-site ordering of the perovskite support material, as a result of the dielectric engineering carried out to promote the nucleation of Pt nanoparticles at its surface. As such, this work displays the importance of atomic-scale structural and chemical analyses in understanding electrocatalytic systems and provides insights into the possibilities of dielectric engineering in performance optimization.

2. Results and Discussion

Ti-doping of the $BaMnO_3$ system to give $BaTi_{0.5}Mn_{0.5}O_3$ was carried out using a hydroxide composite-mediated method, as described in the Experimental Section.[37] This process involves mixing the two B-site metallic oxides with the A-site metallic salt and heating them in a molten eutectic hydroxide mixture. This approach does not rely on the use of high temperatures and pressures, thus providing a simple, versatile, cost-effective, and more environmentally friendly way of synthesizing mixed transition-metal perovskites. In fact, the low temperature (200 °C) and pressures (closed vessel at atmospheric pressure) associated with this method are in stark contrast to the harsh synthesis conditions traditionally used during the solid-state synthesis of perovskite materials. The possible reaction mechanism of this synthesis, which is carried out in NaOH and KOH, can be described as follows[38]

$$BaCl_2 + 2NaOH \rightarrow Ba(OH)_2 + 2NaCl \quad (2)$$

$$0.5MnO_2 + 0.5TiO_2 + 2NaOH \rightarrow Na_2\left(Ti_{0.5}Mn_{0.5}\right)O_3 + H_2O \quad (3)$$

$$Ba(OH)_2 + Na_2\left(Ti_{0.5}Mn_{0.5}\right)O_3 \rightarrow Ba\left(Ti_{0.5}Mn_{0.5}\right)O_3 + 2NaOH \quad (4)$$

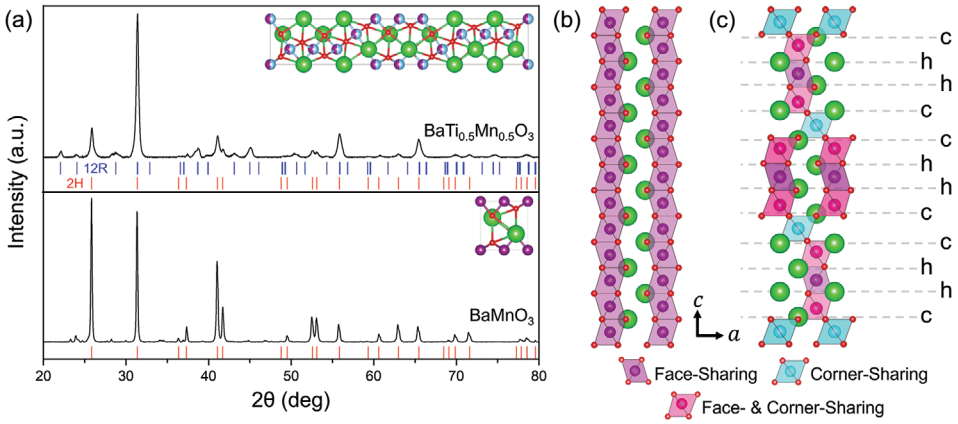

Figure 1. Structural analysis of $BaMnO_3$ and $BaTi_{0.5}Mn_{0.5}O_3$. a) Experimental XRD patterns of as-synthesized $BaMnO_3$ (lower panel) and $BaTi_{0.5}Mn_{0.5}O_3$ (upper panel). The ticks below the experimental patterns represent the positions of the reference peaks from the 2H (red) and 12R (blue) perovskite structures. The unit cells of 2H-$BaMnO_3$ and 12R-$BaTi_{0.5}Mn_{0.5}O_3$ are shown in the insets with Ba, Ti, Mn, and O atoms in green, blue, purple, and red, respectively. Structural model of b) $BaMnO_3$ and c) $BaTi_{0.5}Mn_{0.5}O_3$, with the face-sharing, corner-sharing and face- and corner-sharing BO_6 octahedra shown in purple, blue and pink, respectively. In c) the cubic and hexagonal layering of the BO_3 layers are denoted with the letters c and h, respectively.

where NaOH can be replaced with KOH. From this, it is clear that the choice of a eutectic mixture of NaOH and KOH as the molten salt medium not only allows for a low reaction temperature (eutectic point at 167 °C) but also facilitates the reaction mechanism by acting as an active component and oxygen donor.[39–41] The crystal structure of as-synthesized $BaMnO_3$ and $BaTi_{0.5}Mn_{0.5}O_3$ are characterized and compared in **Figure 1a**. The X-ray diffraction (XRD) pattern of $BaMnO_3$ reveals a high degree of phase purity with peaks well-indexed to the 2H-hexagonal perovskite crystal structure (JCPDS no. 26–0168) with space group $P6_3/mmc$ and lattice parameters $a = b = 5.6991$ and $c = 4.8148$ Å. Alternatively, the XRD pattern of $BaTi_{0.5}Mn_{0.5}O_3$ cannot be assigned to a single phase. Considering the possible polymorphs exhibited by different $BaTi_xMn_{1-x}O_3$ material systems, a combination of the 2H-hexagonal and 12R-rhombohedral perovskite structures successfully matches all observed peaks. The 12R-rhombohedral perovskite structure (JCPDS no.74-0646) with space group $R\bar{3}m$ and lattice parameters $a = b = 5.6914$ and $c = 27.9186$ Å are consistent with other reports of $BaTi_{0.5}Mn_{0.5}O_3$ despite the contrasting synthesis routes.[42–44] In $BaMnO_3$, the perovskite structure is based solely on the hexagonal close-packing of the BaO_3 layers with continuous chains of face-sharing MnO_6 octahedra along the *c*-axis, as shown in Figure 1b. This leads to the formation of a two-layer hexagonal cell denoted by 2H. Before proceeding further, it is important to note that $BaTiO_3$, the other end-group of the $BaTi_xMn_{1-x}O_3$ perovskite system, exhibits a structure consisting of cubic close-packed arrays of BaO_3 layers, such that all TiO_6 octahedra are corner-sharing. As a result, the $BaTi_xMn_{1-x}O_3$ perovskite system can exhibit various structural polytypes that are formed by the intergrowth of cubic and hexagonal BaO_3 layers. Therefore, depending on the stacking sequence of these layers, a variety of corner- and face-sharing BO_6 octahedral units exist along the *c*-axis. In such polytypes, the unit cell is determined by the number of AO_3 layers *n* with the symbols H and R used to represent the symmetry. From this, the 12R perovskite structure displayed by $BaTi_{0.5}Mn_{0.5}O_3$ consists of a total of 12 BaO_3 close-packed layers with a $(hhcc)_3$ stacking sequence, such that strings of three face-sharing BO_6 octahedra are connected by a corner-sharing octahedron, as shown in Figure 1c. This is consistent with an increase in the average B-site cation size due to the incorporation of Ti, resulting in a lower Goldschmidt tolerance factor ($t = r_A + r_O)/\sqrt{2}(r_B + r_O)$), and the formation of cubic layers with corner-sharing octahedra.[44] Although $BaTi_{0.5}Mn_{0.5}O_3$ can be indexed to the 12R and 2H phases, peak broadening is observed in the XRD pattern, which is indicative of some type of disorder within the crystal structure—a phenomenon that will be explored locally using electron microscopy techniques.[45]

Transmission electron microscopy (TEM) imaging was performed to investigate the as-synthesized morphology of $BaTi_{0.5}Mn_{0.5}O_3$ and to further confirm its crystallinity and structure. From the low magnification TEM image in **Figure 2a** $BaTi_{0.5}Mn_{0.5}O_3$ exhibits a tapered rod-like morphology, in which the diameter of the rod decreases toward its ends. While the morphology of $BaMnO_3$ is also rod-like, the diameter of the rods stays consistent throughout their lengths.[37] Thus, the addition of Ti into the $BaMnO_3$ system causes shortening and tapering of the rods, which is consistent with previous reports of $BaMnO_3$ and $BaTi_{0.5}Mn_{0.5}O_3$ synthesized via a similar hydroxide composite-mediated method.[38,46] Additionally, some rods taper to multiple points at their ends, as shown by the representative TEM images in Figure S1 (Supporting Information). The high-resolution transmission electron microscopy (HRTEM) images and corresponding fast Fourier transforms (FFT) in Figure 2b,c reveal the crystallinity and growth modality of the tapered rods. Complementary to the XRD pattern in Figure 1, the lattice fringes in the HRTEM image can be indexed to the 12R-rhombohedral perovskite structure of $BaTi_{0.5}Mn_{0.5}O_3$. In fact, imaging from the $[01\bar{1}0]$ or $[0\bar{1}10]$ zone axes means viewing the structure parallel to the columns of BaO_3 close-packed layers, such that the $(hhcc)_3$ stacking sequence in the 12R perovskite structure is evident, as marked on the inset of Figure 2b. The presence of the 12R-rhombohedral perovskite structure is further confirmed by the selected area electron diffraction (SAED) patterns in Figure S2 (Supporting Information). By indexing the

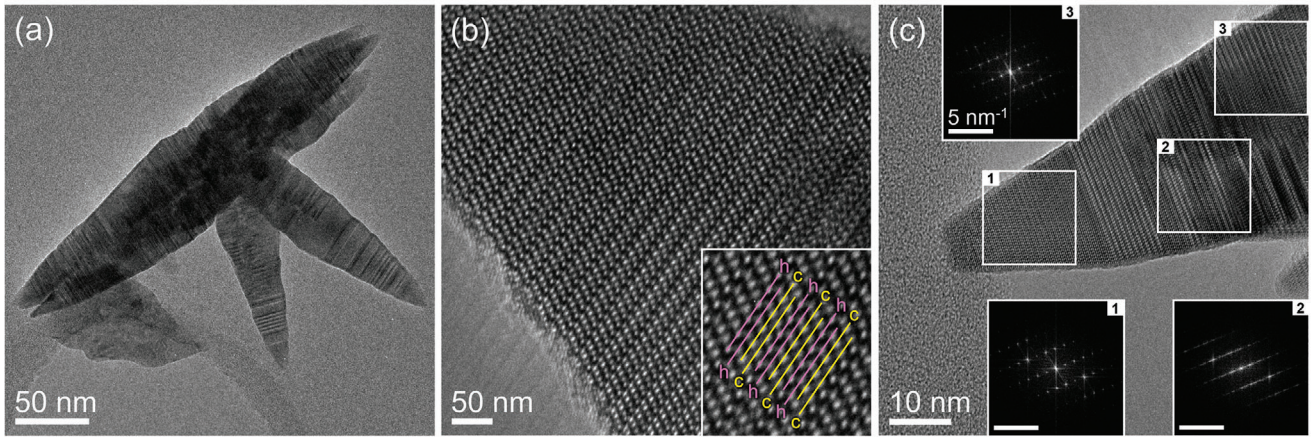

Figure 2. Perovskite $BaTi_{0.5}Mn_{0.5}O_3$ morphology and crystallography. a) Low magnification TEM image of $BaTi_{0.5}Mn_{0.5}O_3$ tapered rods. b) HRTEM image of $BaTi_{0.5}Mn_{0.5}O_3$ displaying the 12R-rhombohedral perovskite structure from the $[0\bar{1}10]$ zone axis. The inset image is magnified to outline the $(hhcc)_3$ stacking sequence of the 12R structure, with hexagonal (h) and cubic (c) BaO_3 layers marked in pink and yellow, respectively. c) TEM image and corresponding FFTs for domains 1, 2, and 3.

planes identified in the HRTEM image, a growth direction of [0001] along the length of the tapered rods can be determined, which is as expected since there is an inherent crystallographic anisotropy along the *c*-direction associated with the 12R perovskite structure. While Figure 2b exemplifies the regular 12-layer stacking sequence characteristic of the 12R structure, the HRTEM image and corresponding FFTs in Figure 2c explore the extent of ordering and regularity of the stacking sequence in $BaTi_{0.5}Mn_{0.5}O_3$. By examining the corresponding FFTs, areas 1 and 3, which show characteristic spot patterns, are well indexed with the 12R perovskite structure, and are associated with areas of regular ordering and stacking. On the other hand, the FFT corresponding to area 2 consists of diffuse streaks along the [0001] direction, indicating disruption to the ordered layering along the *c*-axis. This is a result of the presence of planar faults due to the intergrowth of different polytypes and variation from the $(hhcc)_3$ stacking sequence.[44,45] This disordered atomic structure is consistent with the broader maxima observed in the XRD pattern for $BaTi_{0.5}Mn_{0.}5O3$ in Figure 1 and will be investigated further using atomic resolution STEM imaging. Returning to areas 1 and 3, it is important to note that while area 1 is imaged from the $[0\bar{1}10]$ zone axis, area 3 is imaged from the $[01\bar{1}0]$ zone axis meaning that the crystallographic domains are tilted 180° to one another about the *c*-axis. In this case, the two tilted domains are separated by a region of disordered atomic structure. However, as evident from the SAED pattern in Figure S2b (Supporting Information), two domains tilted at 180° to one another about the *c*-axis can coexist without the presence of any intermediate disordered layers, which is indicated by the absence of diffuse streaks along the [0001] direction in the SAED. This occurs when the stacking sequence is reflected about a singular hexagonal layer, as displayed in Figure S2c (Supporting Information).[44] This structural motif will be directly evidenced using atomic resolution STEM imaging. In addition to the exhibition of the 12R-rhombohedral perovskite structure, XRD also shows the presence of the 2H-hexagonal perovskite structure in $BaTi_{0.5}Mn_{0.5}O_3$. However, it is important to note that while the 2H and 12R structures coexist within the same rods, not all rods display the 2H structure. When they do, typically the two structures are joined together by a region of irregular stacking, as confirmed by the HRTEM images and corresponding FFTs in Figure S3 (Supporting Information). Generally, rods that incorporate the 2H perovskite structure have extended regions where the diameter of the rod does not change, thus the 12R perovskite structure forms at the ends of the rod where the diameter can decrease, causing the rod to taper.

Atomic-resolution high-angle annular dark field (HAADF) STEM imaging was used to confirm the atomic structure of $BaTi_{0.5}Mn_{0.5}O_3$ tapered rods and to further investigate the irregularity of the crystallographic stacking sequence. HAADF STEM imaging is often termed Z-contrast imaging as it leads to image contrast that is highly dependent on the atomic number ($Z^{\sim 2}$) of the scattering element.[47] Therefore, by examining the HAADF STEM images in **Figure 3**, the positions of the Ba, Ti, and Mn atoms within the planes can be deduced, with the Ba atoms appearing brighter due to their heavier atomic weight. Although the O atoms are too light to be detected in such images, due to the insensitivity of this imaging technique to light elements, the 12R perovskite structure is still apparent by examining the atomic positions of the other elements.[48] The larger field of view of the atomic structure in Figure 3a allows for the structural variation from the regular 12R stacking sequence to become clear, as outlined in Figure S4a (Supporting Information). While there are extended regions of the 12R structure, disruptions to the regular stacking sequence in the *c*-direction are present in the form of missing and extra BaO_3 hexagonal planes, as well as extended regions of hexagonal stacking (like the 2H structure) which may feature cubic BaO_3 planes at random. This irregularity is also denoted in Figure 3b, in which it is clear that a missing hexagonal plane causes the 12R structure to reflect about a singular hexagonal plane and corresponds to a 180° tilt of the structure about the *c*-axis. Alternatively, the presence of two extra hexagonal planes does not cause the 12R structure to reflect, since the zig-zag arrangement of the Ba atomic columns continues in the same direction. It is important to note that although nearly all tapered rods consist of some irregularity to the 12R structure, caused by

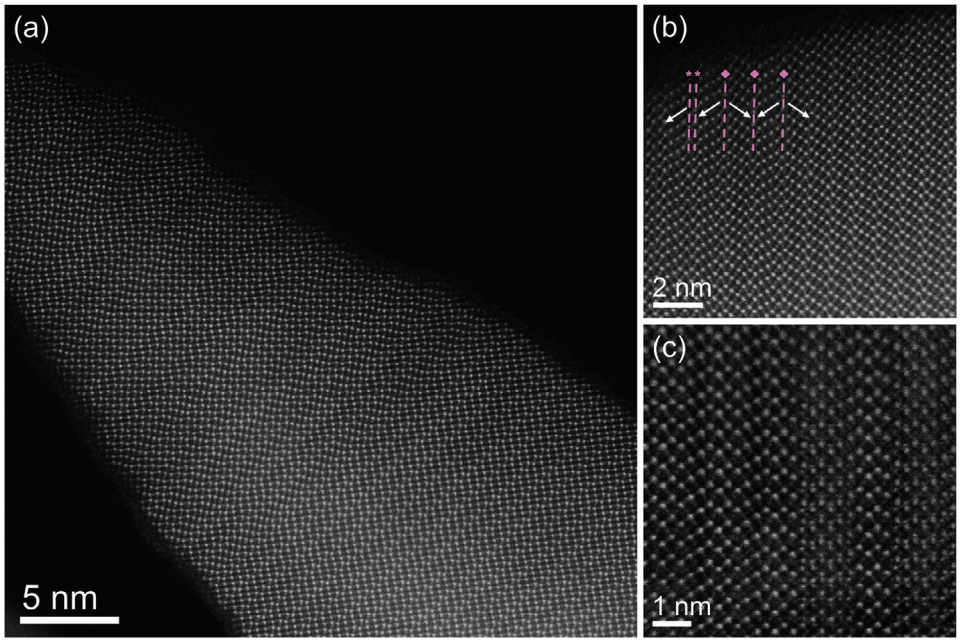

Figure 3. Atomic resolution HAADF STEM images of $BaTi_{0.5}Mn_{0.5}O_3$ tapered rods from the [0$\bar{1}$10] zone axis. In b) the pink dashed lines represent hexagonal BaO_3 layers. Those marked with a diamond (◆) represent single hexagonal layers about which the 12R structure reflects – this corresponds to the removal of a hexagonal layer in the 12R stacking sequence or a 180° tilt of the structure about the *c*-axis. Those marked with an asterisk (*) represent two extra hexagonal layers in the 12R stacking sequence. In c) some regions do not conform to the 12R or 2H perovskite structures.

the intergrowth of cubic and hexagonal BaO_3 layers, the size and sequences of such regions are not consistent across rods. As a result, the irregularity can be considered random on a sample-wide scale. Further to these more easily characterizable structural irregularities, Figure 3c displays the presence of regions in which the structure varies from the simple intergrowth of hexagonal and cubic layers. However, these regions are considered a minority, and hence, will not be discussed further.

As an extension of the structural analysis carried out via XRD, HRTEM, SAED, and STEM, EELS spectrum imaging was used to investigate the presence and positioning of Mn and Ti within the 12R-rhombohedral structure and the other mixed polytypes exhibited by the $BaTi_{0.5}Mn_{0.5}O_3$ system. As mentioned previously, the BO_6 octahedra, and hence the B-sites, are characterized depending on their extent of face-sharing or corner-sharing with neighboring BO_6 octahedral units. As a result, there are three unique B-sites; those that are purely face-sharing are denoted as M1; those that are purely corner-sharing are denoted as M3; and finally, those that have both a face-sharing and corner-sharing connection with neighboring BO_6 octahedra are denoted as M2. Since the two end-groups of the $BaTi_{0.5}Mn_{0.5}O_3$ perovskite system exhibit structures that consist solely of face-sharing ($BaMnO_3$) or corner-sharing ($BaTiO_3$) BO_6 octahedra, it is hypothesized that Mn will preferentially occupy the M1 site, and Ti the M3 site. Conversely, there is no expected preferential filling of the M2 site. From the elemental EELS map in **Figure** 4b, there is a clear distinction between Mn-rich and Ti-rich regions displayed in blue and green, respectively. These regions are found to vary in thickness along the length of the rod, which can ultimately be linked to the variation in the stacking sequences of the BaO_3 layers, as shown in Figure 3 and Figure S4 (Supporting Information). In fact, when an area exhibiting the regular 12R perovskite structure is probed using EELS, the Mn-rich and Ti-rich regions display constant thickness across the structure, as shown by the HAADF STEM image and corresponding elemental map in Figure S5 (Supporting Information). This is consistent with the $(cchh)_3$ stacking sequence of the 12R perovskite structure, which also results in the sequencing of the B-site type such that it follows $(M3, M2, M1, M2)_3$. Alternatively, the thicker Mn-rich regions featured in Figure 4b can be related to extended regions of hexagonal stacking shown by the shaded regions in Figure S4 (Supporting Information). This is consistent with the fact that hexagonal stacking of the BaO_3 layers results in continuous chains of face-sharing BO_6 octahedra along the *c*-direction, and thus consists solely of the M1-type B-site. Further to this, rods that are characterized by both the 2H and 12R structures, exhibit extended Mn-rich regions corresponding to the 2H structure, as shown in Figure S6 (Supporting Information). This is consistent with the fact that the 2H-hexagonal perovskite structure is the atomic structure exhibited by the $BaMnO_3$ end-group.[37] As discussed during the structural analysis, generally the 2H and 12R structures are joined together by a region of irregular stacking caused by the intergrowth of hexagonal and cubic layers. This is also seen during the elemental analysis in Figure S6 (Supporting Information). Moving from left to right across the elemental map, the thickness of the Mn-rich and Ti-rich layers varies before becoming more constant due to the irregular intergrowth of cubic and hexagonal layers before forming the regular 12R $(cchh)_3$ stacking sequence. Taking the elemental analysis one step further, higher magnification EELS spectrum imaging allows for the direct mapping and identification of the M1, M2, and M3 sites, as shown by the HAADF STEM images and EELS elemental maps

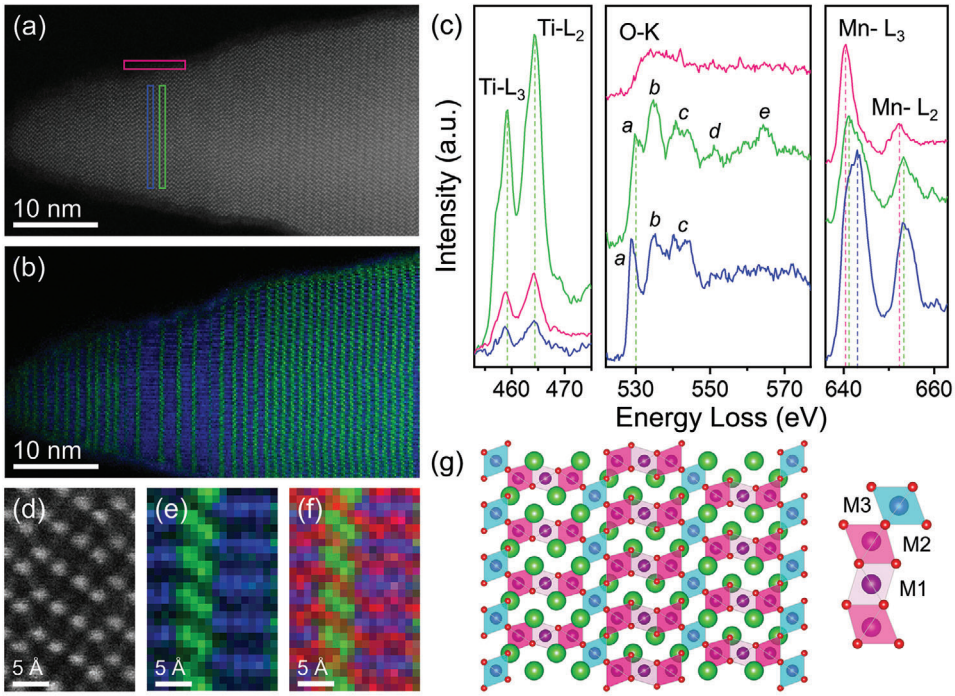

Figure 4. Elemental and chemical analysis of $BaTi_{0.5}Mn_{0.5}O_3$. a) HAADF STEM image and b) corresponding elemental map of the Mn L-edge (blue) and Ti L-edge (green). c) Spatially resolved Ti $L_{3,2}$-edge, O K-edge, and Mn $L_{3,2}$-edge EELS spectra from Mn-rich (blue) Ti-rich (green) and surface (pink) regions, as marked on the HAADF STEM image in a). All spectra are integrated over 180 pixels, and each spectrum is normalized within its given elemental group (e.g., Ti $L_{3,2}$-edge spectra are normalized to the Ti-rich region spectrum, and Mn $L_{3,2}$-edge spectra to the Mn-rich region spectrum). d) Atomic-resolution HAADF STEM image of $BaTi_{0.5}Mn_{0.5}O_3$ from the [0$\bar{1}$10] zone axis. e) and f) show the corresponding elemental maps with the Mn and Ti L-edges in blue and green, respectively, and the Ba M-edge in red. g) Structural model of the 12R-rhombohedral perovskite structure from the [0$\bar{1}$10] zone axis with the M1, M2, and M3 B-site octahedra marked in purple, pink, and blue, respectively.

in Figure 4d–f. These maps are direct evidence of the preferential filling of the M1 and M3 B-sites with Mn and Ti ions, respectively. Additionally, they show that in some cases the M2 site is filled with Mn ions, whereas in other cases it is filled with Ti ions. The B-site sequence displayed in Figure 4e is M2, M1, M2, M3, M2, M1, M2 which corresponds with the following elemental sequencing Mn, Mn, Ti, Ti, Mn, Mn, Mn (see also Figure S7, Supporting Information). This has previously been proposed via neutron diffraction and valence bond sum calculations.[42–44,49] However, since the latter is theoretical, and the refinement of the former cannot identify the elemental occupancy of the B-sites due to the similar neutron scattering lengths of Mn and Ti ions (Mn = −3.73 fm, Ti = −3.438 fm), the atomic resolution EELS analysis carried out here proves superior in providing direct evidence for the B-site elemental ordering in 12R $BaTi_{0.5}Mn_{0.5}O_3$.[43] B-site ordering plays a crucial role in the interplay between charge, spin, and lattice degrees of freedom in perovskite materials resulting in the display of unique physical phenomena and promising functional properties that cannot be achieved in their cation-disordered counterpart.[50,51] In fact, B-site ordered perovskite materials show potential application in a wide range of devices such as electrically tunable microwave devices, multiferroic solar cells, magneto-optic devices, and spin-filter devices.[52–56] B-site ordering in 12R $BaTi_{0.5}Mn_{0.5}O_3$ causes the formation of magnetic dimers and trimers of Mn ions, coexisting with a population of orphan spins.[42,49] As a result, $BaTi_{0.5}Mn_{0.5}O_3$ presents a rare case of an intrinsically disordered S = 3/2 spin-gap system with a frustrated ground state.[42] However, the magnetic and spin properties of $BaTi_{0.5}Mn_{0.5}O_3$ are outside the scope of this work, and hence will not be discussed further.

Beyond the identification of elemental entities, EELS is a powerful spectroscopic tool with the capability of determining the local electronic state and coordination environment of the atoms or ions present within a material.[57] Therefore, in support of the structural-elemental correlation of $BaTi_{0.5}Mn_{0.5}O_3$ carried out above, EELS was also used to probe the chemical nature of Mn and Ti further. Our previous report found the existence of an amorphous layer at the surface of $BaMnO_3$ rods containing reduced Mn states in the form of Mn^{3+}.[37] With the addition of Ti into the $BaMnO_3$ system, the amorphous layer remains present and is ≈1 nm in thickness, as seen in Figure 4a. Consequently, the amorphous surface layer can be considered an inherent result of the hydroxide-mediated method used to synthesize both $BaMnO_3$ and $BaTi_{0.5}Mn_{0.5}O_3$. Figure 4c displays the spatially resolved Ti $L_{3,2}$-edge, O K-edge, and Mn $L_{3,2}$-edge EELS spectra from the areas marked in Figure 4a using the same colors. The $L_{3,2}$-edges consist of two peaks, L_3 and L_2, on the lower and higher energy loss sides, respectively. They correspond to the energy loss caused by promoting electron transitions from the $2p_{3/2}$ and $2p_{1/2}$ states, respectively, to unoccupied 3d bands, and hence reflect the local environment and oxidation state of the transition metal ion in question.[58] Additionally, the separation between the peaks

reflects the spin-orbit splitting of the initial and final states in the transition.[59] Besides the changes in energy loss associated with the $L_{3,2}$-edge, the L_3/L_2 intensity ratio can be related to the transition metal ion oxidation state, as it is dependent upon the spin-spin coupling and interactions between the initial and final states of the electron transition.[60] Further to the transition metal $L_{3,2}$-edge, the O K-edge and its corresponding energy loss near edge structure (ELNES) prove themselves as useful indicators of the chemical environment and atomic coordination of the transition metal ion, especially when bonded in an octahedral configuration.[61,62] Touching first on the spatially resolved O K-edge EELS spectra in Figure 4c, there is an evident distinction between the corresponding ELNES for the Mn-rich, Ti-rich, and surface areas of the rods. For the Mn-rich area, the O K-edge ELNES is composed of three major regions, which are labeled *a* to *c* and are present as a result of the hybridization of the O 2p orbitals with the Mn 3d, Ba 5d, and Mn 4sp orbitals, respectively.[62–64] Similarly, the O K-edge ELNES for the Ti-rich area features five major regions labeled *a* to *e*, with regions *a* to *c* related to the hybridization between the O 2p orbitals with the Ti 3d, Ba 5d, and Ti 4sp orbitals, respectively.[65,66] In addition, regions *d* and *e* can be related to the scattering at the nearest and outer-lying O shells.[67,68] While the ELNES for Mn-rich and Ti-rich regions have similar origins, it is clear that the fine structures are different and there is a shift in the onset of the pre-edge feature (labeled a) to lower energy for Mn-rich regions. The oscillation of the O K-edge fine structure further clarifies the separation between Mn and Ti in $BaTi_{0.5}Mn_{0.5}O_3$ tapered rods, thus supporting the preferential filling of the different B-site types. Furthermore, the O K-edge corresponding to the surface layer does not exhibit any obvious ELNES, which can ultimately be linked to the lack of long-range order associated with the amorphous nature of this layer.[37] Therefore, the incorporation of Ti in $BaMnO_3$ does not significantly affect the amorphous Mn layer, which is the origin of catalytic activity in the system.

By relating the spatially resolved Mn $L_{3,2}$-egde EELS spectra in Figure 4c to the HAADF STEM image of the mapped area displayed in Figure 4a, there is a clear chemical shift in the Mn L_3 peak between the Mn-rich and Ti-rich regions, with the latter resulting in lower energy loss. Moreover, there is a further shift to lower energy loss when traversing to the amorphous layer at the surface of the rods. Since the effective charge on the metal site increases with oxidation state, a decrease in the energy loss of the $L_{3,2}$-edge can be related to a reduction in the oxidation state of the corresponding metal. This is consistent with the change in Mn L_3/L_2 intensity ratio, which is found to increase with decreasing oxidation state.[69] By comparison of the Mn L_3 and L_2 peak positions with that of $BaMnO_3$ rods, as shown in Figure S8 (Supporting Information), the Mn states within the Mn-rich regions and the amorphous layer can be identified as Mn^{4+} and Mn^{3+}, respectively.[37] Since the Mn L_3 and L_2 peak positions associated with the Ti-rich region are intermediate between that of Mn^{4+} and Mn^{3+} states, the average oxidation state of the Mn ions within this region must fall somewhere between +4 and +3. However, peak positions, and hence average Mn oxidation state, do not seem to be consistent across all Ti-rich regions, as shown in Figure S8 (Supporting Information). In $BaTi_{0.5}Mn_{0.5}O_3$, the Mn ions are in an octahedral environment for which the crystal field splitting results in the formation of t_{2g} and e_g states. Although not completely resolved in this case, the change in the shape of the L_3 peak between that of the Mn-rich and Ti-rich regions may be related to a change in the relative electron occupancy of the t_{2g} and e_g states, since the e_g side of L_3 peak is more prominent in the Mn-rich region and the converse is true for the Ti-rich region. When a similar analysis is carried out on the Ti $L_{3,2}$-edge, it is clear that although there is a slight chemical shift in the L_3 (0.3 eV) and L_2 (0.2 eV) peaks, the magnitude is not large enough to account for the transfer of an electron to the Ti ions which would cause a decrease in the oxidation state.[57] Therefore, despite the variation in the oxidation state of the Mn ions between the Mn-rich, Ti-rich, and surface regions, the Ti oxidation state does not vary from the Ti^{4+} state, identified using the position of the L_3 and L_2 peaks.[70] Instead, the observed shift may reflect differences in core-level energies caused by defects, and/or changes in the overall electronic structure of unoccupied states.[71] In addition to the peak position analysis, Ti $L_{3,2}$-edge EELS spectra recorded from the bulk of $BaTi_{0.5}Mn_{0.5}O_3$ tapered rods display a satellite peak in the ELNES on the higher energy side of the L_2 peak, as highlighted in Figure S9 (Supporting Information). Related to plural scattering, the satellite peaks can be attributed to the backscattering from neighboring atoms, with charge transfer processes dominating the satellite structures.[68] Since the peaks can be explained by charge transfer, their intensities are often increased in oxides due to the transfer of electrons from the transition metal atoms toward the oxygen atoms, thereby increasing the number of empty states at the metal atoms.[72,73] Therefore, the absence of such satellite peaks from the surface Ti $L_{3,2}$-edge spectrum indicates the lack of charge transfer processes between Ti and O atoms, which is consistent with the absence of fine structure from the O K-edge, and hence the amorphous nature, and lack of long-range order in the surface layer. Furthermore, it is important to note that while the surface layer consists of reduced Mn states, it also contains Ti, O, and Ba as indicated by the EELS spectra and maps in Figure S6 (Supporting Information).

In our previous study, $BaMnO_3$ rods exhibited activity for the ORR due to the presence of Mn^{3+} states at their surface.[37] As a result, $BaMnO_3$ can be categorized as a useful candidate to support Pt nanoparticles, thus promoting the activity of the perovskite system while keeping costs lower when compared with the benchmark Pt/C catalyst. In saying that, the heterogenous nucleation of Pt nanoparticles at the surface of $BaMnO_3$ rods proved unsuccessful via microwave heating, as shown in Figure S10 (Supporting Information). For this reason, Ti was introduced into the $BaMnO_3$ perovskite system to tune its dielectric properties, and ultimately promote the heterogeneous nucleation of Pt nanoparticles at its surface, whilst maintaining the presence of Mn^{3+} surface states. The dielectric properties of a material can be characterized by the frequency-dependent dielectric permittivity (ε) of the material, which is measured relative to the permittivity of vacuum (ε_0). In general, the dielectric permittivity of materials is complex, such that $\varepsilon = \varepsilon' - i\varepsilon''$, where ε' is the real part of the dielectric permittivity (referred to plainly as the dielectric permittivity in this case) and ε'' is the imaginary part, also known as the loss or dissipation factor. As the names suggest, the dielectric permittivity is a measure of the amount of energy that can be stored in a material in the form of electric fields, whereas the dielectric loss factor is a direct measure of how much energy a material can dissipate in the

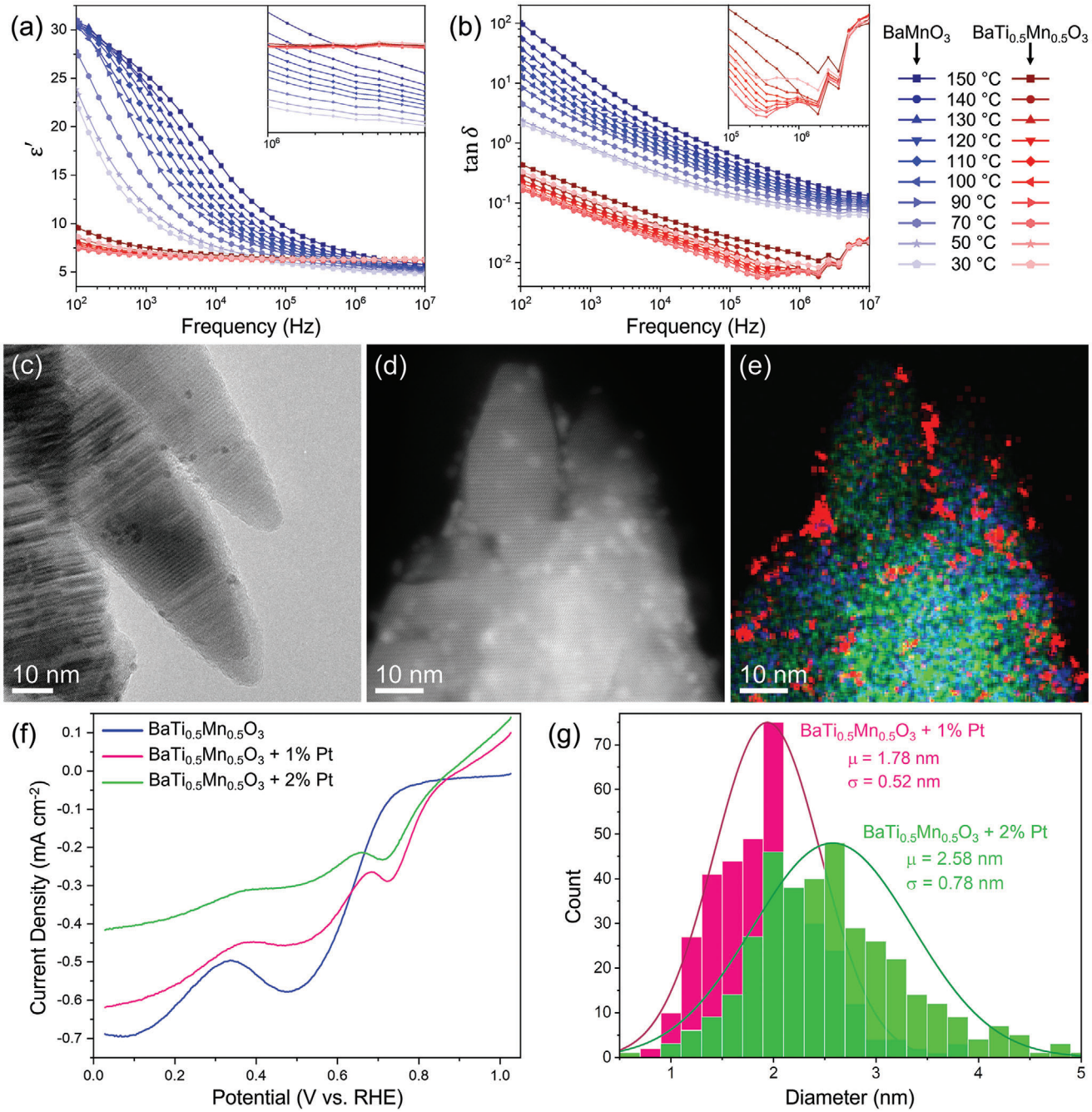

Figure 5. Pt nanoparticle nucleation on $BaTi_{0.5}Mn_{0.5}O_3$ support material. a) Frequency-dependent real part of the dielectric permittivity and b) loss tangent measurements of $BaMnO_3$ and $BaTi_{0.5}Mn_{0.5}O_3$ at various temperatures between 30 and 150 °C. The inset in a) shows the crossover of the dielectric permittivity between $BaMnO_3$ and $BaTi_{0.5}Mn_{0.5}O_3$ in the frequency range of 1 to 10 MHz. The inset in b) displays the loss tangent of $BaTi_{0.5}Mn_{0.5}O_3$ from 100 kHz to 10 MHz. The legend corresponding to the graphs in a) and b) is displayed on the right-hand side. c) TEM image, d) HAADF-STEM image, and e) corresponding EDX elemental map of Pt-loaded $BaTi_{0.5}Mn_{0.5}O_3$, with Mn, Ti, and Pt mapped in blue, green, and red, respectively. f) LSV measurements of pristine $BaTi_{0.5}Mn_{0.5}O_3$, as well as $BaTi_{0.5}Mn_{0.5}O_3$ loaded with 1 and 2% Pt. g) Size distribution of Pt nanoparticles nucleated on $BaTi_{0.5}Mn_{0.5}O_3$ via microwave heating with weight loading regimes of 1 and 2%.

form of heat. Although related to the loss factor, the loss tangent (tan δ) is typically recorded instead and is given by $\tan\delta = \varepsilon''/\varepsilon'$. **Figure** 5a,b show the frequency dependence of the dielectric permittivity and loss tangent of $BaMnO_3$ and $BaTi_{0.5}Mn_{0.5}O_3$ at different temperatures. By comparing the two materials, there is an obvious distinction between their dielectric properties. The dielectric permittivity of $BaMnO_3$ exhibits a strong frequency dependence such that it decreases with increasing frequency, and when compared with $BaTi_{0.5}Mn_{0.5}O_3$ it shows a larger temperature dispersion at any selected frequency. In both senses, the

converse is true for $BaTi_{0.5}Mn_{0.5}O_3$ – it displays very little dependence on frequency for the range measured, as well as very little variation with temperature. At low frequencies, $BaMnO_3$ exhibits a larger and more dispersed dielectric permittivity, thus illustrating the greater ability of its dipoles (electronic, ionic, or otherwise) to align with the external electric field. As the frequency increases, the dipoles start to lag behind the field as different polarization mechanisms fail, causing the dielectric permittivity to decrease and become less dispersed.[74–76] At higher frequencies there is a crossover in the magnitude of the dielectric permittivity between $BaMnO_3$ and $BaTi_{0.5}Mn_{0.5}O_3$, as shown in the inset of Figure 5a, such that the dipoles of $BaTi_{0.5}Mn_{0.5}O_3$ can more easily align with the external electric field compared to $BaMnO_3$ within the higher frequency range. This may be related to the size of the dipoles present within the materials, since large, medium, and small-sized electrical dipoles contribute to the dielectric response at low, medium, and high frequencies, respectively.[77] The overall low dielectric permittivity of $BaTi_{0.5}Mn_{0.}5O_3$ ($\varepsilon' < 10$) may be attributed to the presence of disorder in the microstructure in the form of stacking faults and the intergrowth of cubic and hexagonal layers, as revealed by HRTEM and STEM images.[44] In addition to the dielectric permittivity, a comparison between the loss tangent of $BaMnO_3$ and $BaTi_{0.5}Mn_{0.5}O_3$ sheds light on a very important distinction between the materials. The loss tangent of $BaMnO_3$ shows a decrease with increasing frequency, with no evidence of relaxation mechanisms. Conversely, there is clear proof of the presence of relaxation mechanisms in $BaTi_{0.5}Mn_{0.5}O_3$ at high frequencies due to the presence of three peaks above 100 kHz. The maxima of these peaks do not shift with temperature, indicating a non-thermally activated behavior. Generally, the dielectric loss of perovskite materials includes intrinsic and extrinsic losses, where the former refers to the vibration anharmonicity of the perfect lattice and the latter arises from factors including porosity, phase, defects, and site order.[78–80] The intrinsic losses are strongly influenced by the symmetry of the crystal system, such that crystals belonging to different symmetry groups have very different temperature and frequency dependencies associated with the loss tangent.[81,82] A similar loss tangent dependence is seen for different defect types.[82] Therefore, since $BaMnO_3$ and $BaTi_{0.5}Mn_{0.5}O_3$ exhibit hexagonal and rhombohedral crystal symmetries, respectively, with the presence of planar faults in the latter, such crystallographic differences may account for the variation in the loss response between the two materials. For $BaTi_{0.5}Mn_{0.5}O_3$, extrinsic losses are likely to play an additional factor since the dielectric loss is highly sensitive to B-site ordering.[78,80] As a final consideration, partially filled d orbitals can contribute to relaxation mechanisms due to electronic conductivity.[79] As a result, the larger variation in the d orbital filling of $BaTi_{0.5}Mn_{0.5}O_3$ compared to $BaMnO_3$ may also account for the differences in the dielectric loss response.

The heterogeneous nucleation of Pt nanoparticles on the surface of $BaTi_{0.5}Mn_{0.5}O_3$ was carried out via the microwave heating of the support material in the presence of a Pt salt (H_2PtCl_6) at 120 °C. Ethylene glycol was chosen as the reaction medium due to its high boiling point, high dielectric loss, and its ability to play the role of solvent, as well as a stabilizer and reducing agent in the reduction of noble metal salts (e.g., $Pt^{4+} \rightarrow Pt^0$).[32,83,84] The TEM image, HAADF STEM image, and corresponding EDX elemental map in Figure 5c–e, respectively, provide evidence for the successful nucleation of Pt nanoparticles at the surface of $BaTi_{0.5}Mn_{0.5}O_3$ tapered rods. As evidenced by the HRTEM image in Figure S11 (Supporting Information), the Pt nanoparticles are crystalline in nature, displaying a face-centered cubic crystal structure with space group $Fm\bar{3}m$ and lattice parameters $a = b = c = 3.9237$ Å. Therefore, given the correct dielectric properties of the support material, microwave heating provides the ability to heterogeneously nucleate crystalline Pt nanoparticles on the surface of metal oxide support materials within minutes. The ORR performance of pristine and Pt-loaded $BaTi_{0.5}Mn_{0.5}O_3$ samples was evaluated by linear sweep voltammetry (LSV) measurements, as shown in Figure 5f. Corresponding LSVs recorded in nitrogen-degassed electrolytes are included in Figure S13 (Supporting Information), to confirm that the measured activity is due to the reduction of oxygen and not any other reaction. Furthermore, the performance of pristine $BaTi_{0.5}Mn_{0.5}O_3$ was compared to that of $BaMnO_3$, Figure S14 (Supporting Information), to confirm that the addition of Ti in the perovskite system does not significantly deteriorate the ORR performance. This coincides well with the STEM-EELS analysis carried out above, which revealed the presence of the desired Mn^{3+} states at the surface of $BaTi_{0.5}Mn_{0.5}O_3$ tapered rods. Upon examination of Figure 5f, there is no surprise that the ORR onset potential of Pt-loaded $BaTi_{0.5}Mn_{0.5}O_3$ is superior to that of pristine $BaTi_{0.5}Mn_{0.5}O_3$, which has a half potential of 0.647 V versus RHE (reversible hydrogen electrode, against which all potentials in this manuscript are reported). That being said, it may be surprising that the onset potential of samples loaded with 2% Pt is inferior to those loaded with 1% Pt, with half-wave potentials of 0.778 and 0.790 V versus RHE, respectively. Additionally, the samples can be compared using their potential at a standard current density of −0.1 mA cm^{-2}. The same trend prevails with potentials equal to 0.712, 0.810, and 0.794 V versus RHE for pristine, 1% Pt-loaded, and 2% Pt-loaded $BaTi_{0.5}Mn_{0.5}O_3$, respectively. Following the comparison of the nanoparticle size distributions for the 1 and 2% weight-loaded samples in Figure 5g, it becomes clear why the ORR onset potential and activity of the former prove superior despite the lower weight-loading percentage. For $BaTi_{0.5}Mn_{0.5}O_3$ loaded with 1% Pt, the nanoparticles display a smaller mean diameter and lower spread in overall size when compared with that of the higher weight loading regime. This results in a higher electrochemical active surface area associated with the Pt nanoparticles, and hence accounts for the better ORR performance. A comparison of the TEM images in Figure S12 (Supporting Information), shows that in addition to their larger size, the Pt nanoparticles in the 2% weight loading regime often aggregate to form clumps, thus further reducing the active surface area and supporting the higher activity of $BaTi_{0.5}Mn_{0.5}O_3$ with 1% Pt. Therefore, increasing the Pt salt concentration during the nucleation process proves undesirable, since it not only increases the weight loading (higher cost), but also causes the nanoparticle size to increase, and enhances the likelihood of particle aggregation. Consequently, reducing the Pt salt concentration allows for a cost reduction, as well as the nucleation of well-dispersed fine Pt nanoparticles on the metal oxide support. Furthermore, the discrepancy between the current produced by pristine and Pt-loaded $BaTi_{0.5}Mn_{0.5}O_3$ is discussed in the Supporting Information, where post-mortem TEM studies are also carried out

to investigate the stability of Pt nanoparticles on $BaTi_{0.5}Mn_{0.5}O_3$ surfaces.

3. Conclusion

The dielectric engineering of the $BaMnO_3$ perovskite system was carried out using Ti-doping. Crystalline tapered nanorods of $BaTi_{0.5}Mn_{0.5}O_3$ were synthesized via a simple, cost-effective, and environmentally friendly method. The pristine perovskite rods displayed the 12R-rhombohedral structure with signatures of the 2H-hexagonal structure, as well as disordered iterations of the 12R structure resulting from the intergrowth of cubic and hexagonal BaO_3 layers. STEM-EELS analysis directly revealed the preferential occupancy of the face-sharing M1 and corner-sharing M3 B-sites with Mn and Ti, respectively. Dielectric measurements identified differences between the dielectric constant and loss tangent of $BaMnO_3$ and $BaTi_{0.5}Mn_{0.5}O_3$, thus accounting for the ability to heterogeneously nucleate Pt on the latter and not the former via microwave heating. A lower weight loading regime of 1% Pt on $BaTi_{0.5}Mn_{0.5}O_3$ displayed a more advantageous ORR performance due to the smaller size and better dispersion of the Pt nanoparticles, and thus a higher electrochemically active surface area.

4. Experimental Section

$BaMnO_3$ and $BaTi_{0.5}Mn_{0.5}O_3$ Synthesis: $BaMnO_3$ rods were synthesized via a low-temperature, low-pressure, hydroxide composite-mediated method as previously reported.[37] This synthesis method, which was based on a reaction between the precursor metallic salt and metallic oxides in a molten hydroxide solution, was altered to produce $BaTi_{0.5}Mn_{0.5}O_3$ tapered nanorods. The reaction time was increased incrementally during the optimization process starting with 24 h, (the reaction time required to synthesize $BaMnO_3$) and ending with a final reaction time of 99 h. All other reaction conditions remained the same during the optimization process, and the final synthesis method can be described as follows: A 20 g mixture of NaOH and KOH, with a molar ratio 51.5:48.5, was placed in a Teflon vessel. Stoichiometric amounts of TiO_2, MnO_2, and $BaCl_2$ were added to the vessel which was covered and shaken to ensure uniform mixing of the reactants. The reaction was carried out in a furnace at 200 °C for 99 h. Once completed, the vessel and its contents were allowed to cool to room temperature inside the furnace. Hot deionized water was used to dissolve the solid hydroxide mixture and release the solid product, which was subsequently washed with hot and room-temperature deionized water via centrifugation until a neutral pH was reached. The washed product was dried in air at 75 °C for 6 h.

Heterogeneous Nucleation of Pt Nanoparticles on $BaTi_{0.5}Mn_{0.5}O_3$: Pt nanoparticles were heterogeneously nucleated on $BaTi_{0.5}Mn_{0.5}O_3$ tapered rods via a rapid microwave-based method to give weight loadings of 1 and 2%. This method is based on the reduction of a metallic salt using microwave radiation, which allows for the fast and uniform heating of the reaction medium and nanorod support. All nucleation experiments in this study were carried out in 10 mL sealed reaction vials using a CEM Discover-SP microwave system operated at a frequency of 2.54 GHz, a maximum power of 200 W, and fitted with a fiber optic probe to measure temperature. For $BaTi_{0.5}Mn_{0.5}O_3$ with 1% Pt, 20 mg of the as-synthesized $BaTi_{0.5}Mn_{0.5}O_3$ powder and 0.42 mg of H_2PtCl_6 (0.2 mg Pt) were dispersed in 5 mL ethylene glycol by ultrasonication. The solution was heated to 120 °C in the microwave system and held at this temperature for 5 min. Once completed, the vial and its contents were cooled to 50 °C within the microwave chamber by flowing nitrogen gas over the outer walls of the vial. The vial was allowed to cool to room temperature outside of the microwave chamber before the product was sequentially washed with isopropyl alcohol and deionized water and dried at 50 °C for 4 h. The same procedure was carried out for $BaTi_{0.5}Mn_{0.5}O_3$ with 2% Pt, but instead, 0.84 mg of H_2PtCl_6 (0.4 mg Pt) was used.

Characterization: Crystalline phase identification was carried out by powder X-ray diffraction (XRD) using a Bruker D8 Discover diffractometer with a Cu Kα radiation source, Goeble mirror, and Ge double bounce monochromator. For electron microscopy, the samples were added to deionized water and ultrasonically dispersed. A drop of the resulting dispersion was deposited on a lacey carbon-coated Cu grid. Morphological and structural analysis was carried out using transmission electron microscopy (TEM) imaging, selected-area electron diffraction (SAED), and high-resolution transmission electron microscopy (HRTEM) on an FEI Titan 80–300 dual TEM/STEM operated at 300 kV. Atomic-scale scanning transmission electron microscopy (STEM) imaging and electron energy loss spectroscopy (EELS) experiments were performed on a Nion UltraSTEM operated at 200 kV and equipped with a Gatan Enfinium EELS spectrometer. The spectra were acquired and processed using Gatan Digital Micrograph with a dispersion of 0.25 eV ch^{-1}, a collection angle β = 40 mrad, and an exposure time of 20 ms px^{-1}. STEM images and corresponding energy dispersive X-ray spectroscopy (EDX) analysis were carried out on an FEI Titan 80–300 dual TEM/STEM operated at 300 kV and equipped with a Bruker QUANTAX XFlash 6T-30 30 mm^2 EDX detector. The spectra were acquired and analyzed using Bruker ESPIRIT software with a 3.91 Å pixel size, and an exposure time of 15 ms px^{-1} and two spectra recorded at each pixel.

Dielectric Measurements: Complex dielectric permittivity measurements were carried out using a Novocontrol Technologies GmbH & Co. broadband Alpha high-resolution dielectric analyzer in the frequency range 100 Hz to 10 MHz. Small pellets of $BaMnO_3$ and $BaTi_{0.5}Mn_{0.5}O_3$ powders were sandwiched between brass electrodes with a diameter of 10 mm. The temperature of the sample was varied in steps of 1 °C under the application of a weak probe voltage of 0.1 V. The dielectric spectra were recorded at each temperature, which was stabilized within the limit of 0.02 °C. The WINFIT software was utilized to fit the spectra to the Havriliak–Negami equation and obtain the required dielectric.

Electrochemical Measurements: Electrochemical measurements for the as-synthesized and Pt-loaded $BaTi_{0.5}Mn_{0.5}O_3$ samples were conducted in a typical three-electrode system on a Gamry workstation at room temperature. A carbon rod and Hg/HgO electrode were used as the counter and reference electrodes, respectively, with 1 M NaOH as the electrolyte. To prepare the working electrode 10 mg of the relevant $BaTi_{0.5}Mn_{0.5}O_3$ powder was ultrasonically dispersed in a solution containing 450 µL of deionized water, 450 µL of isopropyl alcohol, and 4 µL of Nafion 117 solution. 4 µL of the resulting dispersion was dropcasted on a pre-polished glassy carbon rotating disk electrode with a diameter of 3 mm, and dried in air at 40 °C. Once dry, the electrode was connected to an ALS Co. rotating disk electrode set-up. For each of the active materials, a linear sweep voltammogram (LSV) was recorded without degassing the electrolyte, followed by an LSV recorded in an electrolyte degassed with N_2 for 15 min. All LSVs were recorded at a scan rate of 10 mV s^{-1}, and all potentials were reported against the reversible hydrogen electrode (RHE) using V versus RHE = V versus Hg/HgO + 0.926 V.

Supporting Information

Supporting Information is available from the Wiley Online Library or from the author.

Acknowledgements

The authors acknowledge the Advanced Microscopy Laboratory for the provision of their facilities. Microscopy characterization and analysis have been performed at the CRANN Advanced Microscopy Laboratory (AML) (www.tcd.ie/crann/aml/). The authors wish to thank the support of the ERC CoG, 3D2DPrint (GA 681 544) SFI AMBER (12/RC/2278_P2), and

Frontiers for the Future (20/FFP-A/8950). L.H. would like to acknowledge the support of the IRC through award no. GOIPG/2019/2642. A.R acknowledges funding from SERB (Grant no: SRG/2022/001568). N.Y. thanks the IRC for the award of a postdoctoral fellowship, GOIPD/2021/858. M.P.B. would like to acknowledge the Helmholtz Association's Initiative and Networking Fund (Helmholtz Young Investigator Group VH-NG-1719). This publication has emanated from research supported in part by two grants from Science Foundation Ireland under grant numbers 12/RC/2278_P2 and 20/FFP-A/8950. For the purpose of Open Access, the author has applied a CC BY public copyright license to any Author Accepted Manuscript version arising from this submission.

Open access funding provided by IReL.

Conflict of Interest

The authors declare no conflict of interest.

Data Availability Statement

The data that support the findings of this study are available from the corresponding author upon reasonable request.

Keywords

dielectric engineering, electron energy loss spectroscopy, heterogenous nucleation, oxygen reduction reaction, perovskite, scanning transmission electron microscopy

Received: February 2, 2024
Revised: April 8, 2024
Published online: May 9, 2024

[1] M. N. Islam, A. B. Mansoor Basha, V. O. Kollath, A. P. Soleymani, J. Jankovic, K. Karan, *Nat. Commun.* **2022**, *13*, 6157.
[2] M. Kumar, B. Meena, P. Subramanyam, D. Suryakala, C. Subrahmanyam, *NPG Asia Mater.* **2022**, *14*, 88.
[3] J. Suntivich, H. A. Gasteiger, N. Yabuuchi, H. Nakanishi, J. B. Goodenough, Y. Shao-Horn, *Nat. Chem.* **2011**, *3*, 546.
[4] M. K. Debe, *Nature* **2012**, *486*, 43.
[5] W. Zhou, H. Su, W. Cheng, Y. Li, J. Jiang, M. Liu, F. Yu, W. Wang, S. Wei, Q. Liu, *Nat. Commun.* **2022**, *13*, 6414.
[6] D. Banham, T. Kishimoto, Y. Zhou, T. Sato, K. Bai, J. I. Ozaki, Y. Imashiro, S. Ye, *Sci. Adv.* **2018**, *4*, eaar7180.
[7] R. Zeng, Y. Yang, X. Feng, H. Li, L. M. Gibbs, F. J. DiSalvo, H. D. Abruña, *Sci. Adv.* **2022**, *8*, eabj1584.
[8] Z. W. Seh, J. Kibsgaard, C. F. Dickens, I. Chorkendorff, J. K. Nørskov, T. F. Jaramillo, *Science* **2017**, *355*, eaad4998.
[9] Y. Li, Q. Li, H. Wang, L. Zhang, D. P. Wilkinson, J. Zhang, *Electrochem. Energy Rev.* **2019**, *2*, 518.
[10] K. Yamamoto, T. Imaoka, W. J. Chun, O. Enoki, H. Katoh, M. Takenaga, A. Sonoi, *Nat. Chem.* **2009**, *1*, 397.
[11] H. Jin, Z. Xu, Z. Y. Hu, Z. Yin, Z. Wang, Z. Deng, P. Wei, S. Feng, S. Dong, J. Liu, S. Luo, Z. Qiu, L. Zhou, L. Mai, B. L. Su, D. Zhao, Y. Liu, *Nat. Commun.* **2023**, *14*, 1518.
[12] F. Xiao, Q. Wang, G. L. Xu, X. Qin, I. Hwang, C. J. Sun, M. Liu, W. Hua, H. W. Wu, S. Zhu, J. C. Li, J. G. Wang, Y. Zhu, D. Wu, Z. Wei, M. Gu, K. Amine, M. Shao, *Nat. Catal.* **2022**, *5*, 503.
[13] S. Cherevko, G. P. Keeley, S. Geiger, A. R. Zeradjanin, N. Hodnik, N. Kulyk, K. J. J. Mayrhofer, *ChemElectroChem* **2015**, *2*, 1471.
[14] L. Strandberg, V. Shokhen, M. Luneau, G. Lindbergh, C. Lagergren, B. Wickman, *ChemElectroChem* **2022**, *9*, 202200591.
[15] S. Y. Kang, H. J. Kim, Y. H. Chung, *Nano Convergence* **2018**, *5*, 13.
[16] P. J. Ferreira, G. J. la O', Y. Shao-Horn, D. Morgan, R. Makharia, S. Kocha, H. A. Gasteiger, *J. Electrochem. Soc.* **2005**, *152*, A2256.
[17] H. Schulenburg, B. Schwanitz, N. Linse, G. G. Scherer, A. Wokaun, J. Krbanjevic, R. Grothausmann, I. Manke, *J. Phys. Chem. C* **2011**, *115*, 14236.
[18] K. Tiido, N. Alexeyeva, M. Couillard, C. Bock, B. R. MacDougall, K. Tammeveski, *Electrochim. Acta* **2013**, *107*, 509.
[19] Q. A. Islam, R. Majee, S. Bhattacharyya, *J. Mater. Chem. A* **2019**, *7*, 19453.
[20] B. Kayaalp, S. Lee, L. Nodari, J. Seo, S. Kim, W. Jung, S. Mascotto, *ACS Appl. Nano Mater.* **2020**, *3*, 11352.
[21] M. Kothari, Y. Jeon, D. N. Miller, A. E. Pascui, J. Kilmartin, D. Wails, S. Ramos, A. Chadwick, J. T. S. Irvine, *Nat. Chem.* **2021**, *13*, 677.
[22] H. Li, S. Kelly, D. Guevarra, Z. Wang, Y. Wang, J. A. Haber, M. Anand, G. T. K. K. Gunasooriya, C. S. Abraham, S. Vijay, J. M. Gregoire, J. K. Nørskov, *Nat. Catal.* **2021**, *4*, 463.
[23] G. N. Vayssilov, Y. Lykhach, A. Migani, T. Staudt, G. P. Petrova, N. Tsud, T. Skála, A. Bruix, F. Illas, K. C. Prince, V. r. Matolı´n, K. M. Neyman, J. Libuda, *Nat. Mater.* **2011**, *10*, 310.
[24] J. Hwang, R. R. Rao, L. Giordano, Y. Katayama, Y. Yu, Y. Shao-Horn, *Science* **2017**, *358*, 751.
[25] C. Zhao, X. Zhang, M. Yu, A. Wang, L. Wang, L. Xue, J. Liu, Z. Yang, W. Wang, *Adv. Mater.* **2020**, *32*, 2006145.
[26] M. Risch, *Catalysts* **2017**, *7*, 154.
[27] J. A. Farmer, C. T. Campbell, *Science* **2010**, *329*, 933.
[28] V. T. T. Ho, C. J. Pan, J. Rick, W. N. Su, B. J. Hwang, *J. Am. Chem. Soc.* **2011**, *133*, 11716.
[29] A. Lewera, L. Timperman, A. Roguska, N. Alonso-Vante, *J. Phys. Chem. C* **2011**, *115*, 20153.
[30] W. Chen, G. Qian, Y. Wan, D. Chen, X. Zhou, W. Yuan, X. Duan, *Acc. Chem. Res.* **2022**, *55*, 3230.
[31] W. Chen, W. Fu, X. Duan, B. Chen, G. Qian, R. Si, X. Zhou, W. Yuan, D. Chen, *Engineering* **2022**, *14*, 124.
[32] E. A. Anumol, P. Kundu, P. A. Deshpande, G. Madras, N. Ravishankar, *ACS Nano* **2011**, *5*, 8049.
[33] N. Jain, A. Roy, S. Nair, *Nanoscale* **2019**, *11*, 22423.
[34] R. R. Mishra, A. K. Sharma, *Composites, Part A* **2016**, *81*, 78.
[35] M. Inaba, A. Zana, J. Quinson, F. Bizzotto, C. Dosche, A. Dworzak, M. Oezaslan, S. B. Simonsen, L. T. Kuhn, M. Arenz, *ACS Catal.* **2021**, *11*, 7144.
[36] G. S. Hegde, A. Ghosh, R. Badam, N. Matsumi, R. Sundara, *ACS Appl. Energy Mater.* **2020**, *3*, 1338.
[37] L. Hughes, A. Roy, C. Downing, M. P. Browne, A. Zhussupbekova, I. V. Shvets, V. Nicolosi, *Adv. Funct. Mater.* **2023**, *33*, 2214883.
[38] C. G. Hu, H. Liu, C. S. Lao, L. Y. Zhang, D. Davidovic, Z. L. Wang, *J. Phys. Chem. B* **2006**, *110*, 14050.
[39] G. J. Janz, R. P. T. Tomkins, Physical Properties Data Compilations Relevant ti Energy Storage, U.S. Department of Commerce, **1981**.
[40] S. K. Gupta, Y. Mao, *Prog. Mater. Sci.* **2021**, *117*, 100734.
[41] S. Gopalan, K. Mehta, A. V. Virkar, *J. Mater. Res.* **1996**, *11*, 1863.
[42] F. A. Garcia, U. F. Kaneko, E. Granado, J. Sichelschmidt, M. Hölzel, J. G. S. Duque, C. A. J. Nunes, R. P. Amaral, P. Marques-Ferreira, R. Lora-Serrano, *Phys. Rev. B* **2015**, *91*, 224416.
[43] G. M. Keith, C. A. Kirk, K. Sarma, N. M. Alford, E. J. Cussen, M. J. Rosseinsky, D. C. Sinclair, *Chem. Mater.* **2004**, *16*, 2007.
[44] L. Miranda, A. Feteira, D. C. Sinclair, K. Boulahya, M. Hernando, J. Ramírez, A. Varela, J. M. González-Calbet, M. Parras, *Chem. Mater.* **2009**, *21*, 1731.
[45] L. Miranda, D. C. Sinclair, M. Hernando, A. Varela, J. Ramírez-Castellanos, K. Boulahya, J. M. González-Calbet, M. Parras, *Chem. Mater.* **2010**, *22*, 4320.
[46] H. Liu, C. Hu, Z. L. Wang, *Nano Lett.* **2006**, *6*, 1535.
[47] S. J. Pennycook, L. A. Boatner, *Nature* **1988**, *336*, 565.
[48] E. Yücelen, I. Lazić, E. G. T. Bosch, *Sci. Rep.* **2018**, *8*, 2676.

[49] N. T. Dang, D. P. Kozlenko, T. L. Phan, S. E. Kichanov, N. V. Dang, T. D. Thanh, L. H. Khiem, S. H. Jabarov, T. A. Tran, D. B. Vo, B. N. Savenko, *J. Electron. Mater.* **2016**, *45*, 2477.
[50] P. Ksoll, C. Meyer, L. Schüler, V. Roddatis, V. Moshnyaga, *Crystals* **2021**, *11*, 734.
[51] G. King, P. M. Woodward, *J. Mater. Chem.* **2010**, *20*, 5785.
[52] J. E. Kleibeuker, E.-M. Choi, E. D. Jones, T.-M. Yu, B. Sala, B. A. MacLaren, D. Kepaptsoglou, D. Hernandez-Maldonado, Q. M. Ramasse, L. Jones, J. Barthel, I. MacLaren, J. L. MacManus-Driscoll, *NPG Asia Mater.* **2017**, *9*, e406.
[53] B. Peng, Q. Lu, Y. C. Wang, J. F. Li, Q. Zhang, H. Huang, L. Liu, C. Li, L. Zheng, Z. L. Wang, *Research* **2022**, *2022*, 9764976.
[54] R. Nechache, C. Harnagea, S. Li, L. Cardenas, W. Huang, J. Chakrabartty, F. Rosei, *Nat. Photonics* **2015**, *9*, 61.
[55] H. Das, M. De Raychaudhury, T. Saha-Dasgupta, *Appl. Phys. Lett.* **2008**, *92*, 201912.
[56] M. Bernal-Salamanca, Z. Konstantinović, L. Balcells, E. Pannunzio-Miner, F. Sandiumenge, L. Lopez-Mir, B. Bozzo, J. Herrero-Martín, A. Pomar, C. Frontera, B. Martínez, *Cryst. Growth Des.* **2019**, *19*, 2765.
[57] M. T. Otten, B. Miner, J. H. Rask, P. R. Buseck, *Ultramicroscopy* **1985**, *18*, 285.
[58] L. A. J. Garvie, A. J. Craven, R. Brydson, *Am. Mineral.* **1994**, *79*, 411.
[59] R. F. Egerton, *Electron Energy-Loss Spectroscopy in the Electron Microscope*, Springer, Boston, USA **2011**.
[60] R. D. Leapman, L. A. Grunes, *Phys. Rev. Lett.* **1980**, *45*, 397.
[61] H. Tan, J. Verbeeck, A. Abakumov, G. Van Tendeloo, *Ultramicroscopy* **2012**, *116*, 24.
[62] F. Frati, M. O. J. Y. Hunault, F. M. F. de Groot, *Chem. Rev.* **2020**, *120*, 4056.
[63] S. Kobayashi, Y. Tokuda, T. Mizoguchi, N. Shibata, Y. Sato, Y. Ikuhara, T. Yamamoto, *J. Appl. Phys.* **2010**, *108*, 124903.
[64] M. Varela, M. P. Oxley, W. Luo, J. Tao, M. Watanabe, A. R. Lupini, S. T. Pantelides, S. J. Pennycook, *Phys. Rev. B* **2009**, *79*, 085117.
[65] H. Kurata, S. Isojima, M. Kawai, Y. Shimakawa, S. Isoda, *J. Microsc.* **2009**, *236*, 128.
[66] S. B. Lee, W. Sigle, M. Rühle, *Acta Mater.* **2002**, *50*, 2151.
[67] V. Tileli, M. Duchamp, A. K. Axelsson, M. Valant, R. E. Dunin-Borkowski, N. M. Alford, *Nanoscale* **2015**, *7*, 218.
[68] J. Zhang, A. Visinoiu, F. Heyroth, F. Syrowatka, M. Alexe, D. Hesse, H. S. Leipner, *Phys. Rev. B* **2005**, *71*, 064108.
[69] T. Riedl, T. Gemming, W. Gruner, J. Acker, K. Wetzig, *Micron* **2007**, *38*, 224.
[70] R. Brydson, B. G. Williams, W. Engel, H. Sauer, E. Zeitler, J. M. Thomas, *Solid State Commun.* **1987**, *64*, 609.
[71] S. Stemmer, T. Höche, R. Keding, C. Rüssel, R. Schneider, N. D. Browning, S. K. Streiffer, H. J. Kleebe, *Appl. Phys. Lett.* **2001**, *79*, 3149.
[72] K. Okada, A. Kotani, *J. Electron Spectrosc. Relat. Phenom.* **1993**, *62*, 131.
[73] S. Steinsvik, R. Bugge, J. O. N. GjØNnes, J. TaftØ, T. Norby, *J. Phys. Chem. Solids* **1997**, *58*, 969.
[74] M. Arshad, H. Du, M. S. Javed, A. Maqsood, I. Ashraf, S. Hussain, W. Ma, H. Ran, *Ceram. Int.* **2020**, *46*, 2238.
[75] S. Meher, T. Satpathy, C. Sa, S. Mishra, R. N. P. Choudhary, S. K. Parida, *Mater. Today Proc.* **2022**, *67*, 1103.
[76] D. K. Mahato, A. Dutta, T. P. Sinha, *Bull. Mater. Sci.* **2011**, *34*, 455.
[77] M. Z. M. Halizan, Z. Mohamed, A. K. Yahya, *Sci. Rep.* **2021**, *11*, 9744.
[78] J. Cao, X. Kuang, M. Allix, C. Dickinson, J. B. Claridge, M. J. Rosseinsky, D. M. Iddles, Q. Su, *Chem. Mater.* **2011**, *23*, 5058.
[79] X. Kuang, J. B. Claridge, T. Price, D. M. Iddles, M. J. Rosseinsky, *Inorg. Chem.* **2008**, *47*, 8444.
[80] J. Deng, F. Han, B. Schwarz, M. Knapp, H. Ehrenberg, W. Hua, M. Hinterstein, G. Li, Y. He, J. Wang, Y. Yuan, L. Liu, *Inorg. Chem.* **2021**, *60*, 6999.
[81] V. L. Gurevich, A. K. Tagantsev, *Adv. Phys.* **1991**, *40*, 719.
[82] N. M. Alford, J. Breeze, X. Wang, S. J. Penn, S. Dalla, S. J. Webb, N. Ljepojevic, X. Aupi, *J. Eur. Ceram. Soc.* **2001**, *21*, 2605.
[83] M. V. Danilenko, V. E. Guterman, E. V. Vetrova, A. V. Metelitsa, K. O. Paperzh, I. V. Pankov, O. I. Safronenko, *Colloids Surf. A* **2021**, *630*, 127525.
[84] L. S. Sarma, C. H. Chen, S. M. S. Kumar, G. R. Wang, S. C. Yen, D. G. Liu, H. S. Sheu, K. L. Yu, M. T. Tang, J. F. Lee, C. Bock, K. H. Chen, B. J. Hwang, *Langmuir* **2007**, *23*, 5802.